Transient response and life assessment: Case studies on the load rejection of two hydroelectric turbines

Martin Gagnon and François Léonard

Institut de recherche d'Hydro-Québec – IREQ
1800 boulevard Lionel-Boulet, Varennes, QC, Canada J3X 1S1
{gagnon.martin, leonard.francois}@ireq.ca

Abstract

Transient events often account for most of the fatigue damage sustained by hydroelectric turbines during operation. Since one of these damageable events is load rejection, this paper presents a study of the dynamic response of two hydroelectric turbines during load rejection. The two turbines are similar in design and in overall measured behavior. However, we observed that the two turbine runners exhibit different deformation patterns. As the observed behavior was not expected at the time of the measurement, the result was that some of the available data was under-sampled. To circumvent this, we developed a method to correct the aliased signal in order to obtain suitable rainflow cycle counts and amplitudes for fatigue analysis. The paper presents the methodology used and an overview of the results obtained for both case studies.

1 Introduction

Reliable prediction of structural component fatigue life largely depends on the proper assessment of the severity and variability of the damaging events. In structures such as hydroelectric Francis turbine runners, we observe historically that measurement campaigns rarely account for transient events even if they have a major impact on life expectancy [1-3]. Furthermore, such campaigns are usually carried out only once due to cost and time limitations. One example of a transient event that can generate significant fatigue damage is load rejection. During a load rejection event, the power generated by the turbine runner when the generator is synchronized with the electrical grid is transformed into angular acceleration as soon as the synchronization is lost. The runner then goes into overspeed and the protection system closes the wicket gates at a specific rate in order to limit the water hammer overpressure build-up in the penstock and to stop the runner rotation. The strain response during this transient depends on both the geometry of the runner defined during the design phase and the protection system, which is configured during the commissioning of the runner. Currently, we are unable to predict the runner transient behavior prior to the field measurement campaign. However, the configuration of the protection system could be optimized using field measurements to control the dynamic behavior of the runner during these load rejection transients [2, 4]. Measured strains during load rejection in case study 2 are shown in Figure 1, left. The data presented was assembled to give an overview of the typical operating sequence leading to a load rejection: start-up, synchronization, Speed-No-Load (SNL), production and load rejection. The rainflow cycle count for this loading sequence is presented in Figure 1, right. We observe that the fatigue cycles generated by the load rejection event are significantly larger than those generated by the rest of the operating conditions.

For life assessment of a structure like the hydroelectric turbine runner, two types of flaw need to be considered: surface flaws and embedded flaws. If a simple semi-circular surface flaw as shown in Figure 2 (left) with a radius of 3 mm is used as a basis for comparison between a sequence with and without load rejection, we obtain the propagation results presented in Figure 2 (right). The results are obtained by imposing one start-stop sequence per day with or without one load rejection event per year. We observe that more damage is generated by one load rejection event/year than by a normal start-stop sequence every other day. The propagation results were obtained using a typical BS7910 procedure [5] for both operating sequences.

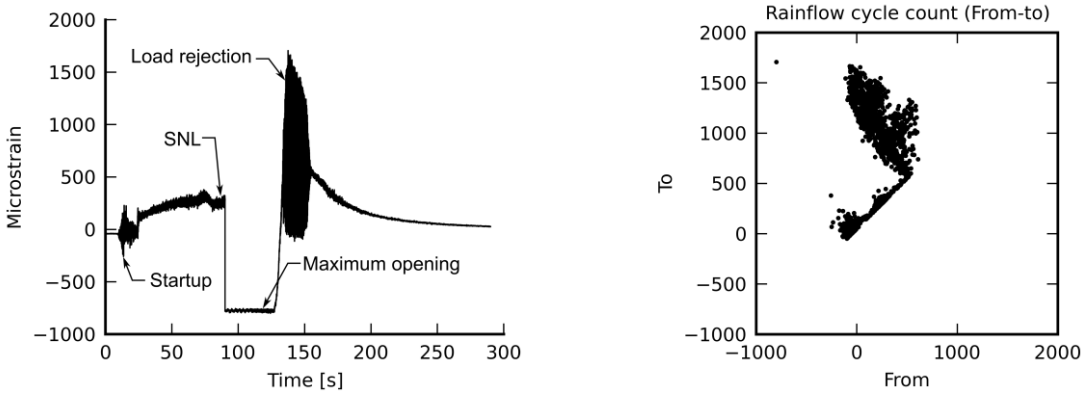

Figure 1: Case study 2: Measured strains on the runner during a maximum opening operating sequence (left); Corresponding rainflow cycle count (right)

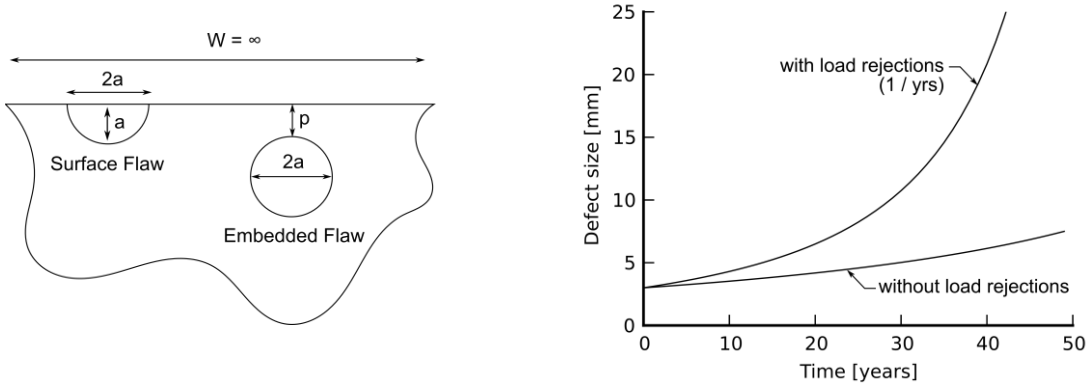

Figure 2: Flaw geometries (left); Propagation results for surface flaws in case study 2 (right).

We notice that even if we consider load rejections to be rare and not part of normal operation, only a few events of the magnitude presented in Figure 1 can control the life expectancy of a hydroelectric turbine runner. Hence, we need to better understand the structure's dynamic behavior in order to develop and validate a suitable numerical model for predicting the runner's response before the measurement campaign during the commissioning of the equipment. The goal of this study is to recover information about the structure's dynamic behavior from the load rejection strain signal measured during the commissioning of two hydroelectric turbines.

The paper is structured as follows. First, we present the two case studies; then, the time-frequency of both case studies is analyzed and the under-sampled signal corrected (case study 2 only); finally, a measurement-to-measurement component phase analysis is carried out to understand the structural dynamic behavior.

2 Overview of the dynamic behavior

In a circular geometry, we expect a circular stationary mode divided into the sum of two modes, one rotating in one direction, the other in reverse. A stationary mode exhibits a phase difference of 0° or 180° between observation points. When the observed differences differ from these values, we can conclude that the vibration mode is not stationary. The fluid-structure coupling therefore preferentially excites one of two overlapping modes and the phase shift between different sensors differs from conventional values of 0° and 180°. This difference can be used to determine the number of nodes of the observed vibratory phenomenon. In our cases, the measurements show a rotary propagating mode having respectively six nodes for case study 1 and seven nodes for case study 2, which is detailed in Section 6. Furthermore, despite the high vibration amplitude measured at the runner by the strain gauges, the phenomenon is not observed in the

turbine guide bearing or in pressure measurements of the spiral case and the draft tube. We therefore consider the phenomenon confined to the runner.

3 Experimental measurements

The first case study is a hydroelectric turbine located in Québec, Canada. This hydroelectric turbine was instrumented with 54 channels including 11 strain gauge channels located on the runner blades. All channels were sampled at 200 samples/s. The second case study is another hydroelectric turbine, also located in Québec, which is similar in design to the first but the turbine in this second case study was instrumented with 97 channels including 12 strain gauge channels located on the runner blades. Also for this case study, the channels connected to sensors located on the electrical generator were sampled at 200 samples/s and all other channels, including strain gauge channels located on the runner blades, were sampled at 100 samples/s. For both case studies, all signals were sampled without an anti-aliasing filter and the recordings were 3 min in length.

On the first turbine runner, the four strain gauges are welded on the high-pressure side of blades 1 and 2 while three strain gauges are welded on blade 9. Since the blade 9 strain gauges had defective cables, their signals were not considered. On the second turbine runner, four gauges are welded on the high-pressure side of blades 3, 9 and 14. In both cases, a polymeric coating was applied in conjunction with metal plates welded on the blade to protect the sensors and wiring.

4 Time-frequency analysis

For each case study, two types of signal are used: strain gauges for blade vibration and gap displacements at the labyrinth at the runner band. Examples of the blade vibration signal for the two case studies can be seen in Figure 3 while Figure 4 shows the time frequency analysis of the vibration signal and Figure 5, the time-frequency analysis of a labyrinth gap displacement. Looking at both the spectrogram from blade vibration and the labyrinth gap displacement, we observe frequency discrepancies generated by the difference between the in-plane vibrations of rotating and static coordinates.

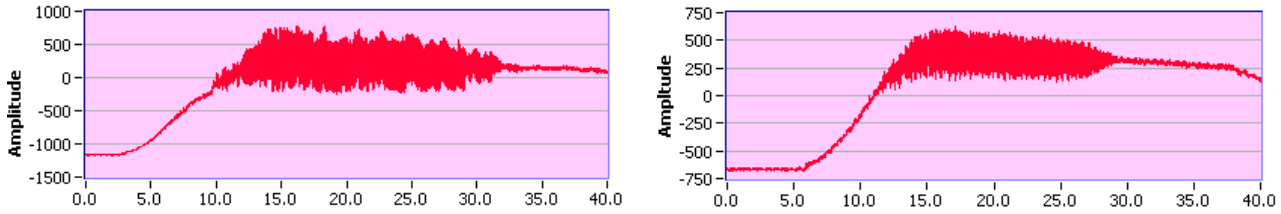

Figure 3: Case study 1 – Strain gauge blade 1, position 2, time signal (με) (left**)**;
Case study 2- Strain gauge signal blade 3, position A, time signal (με) (right**)**.

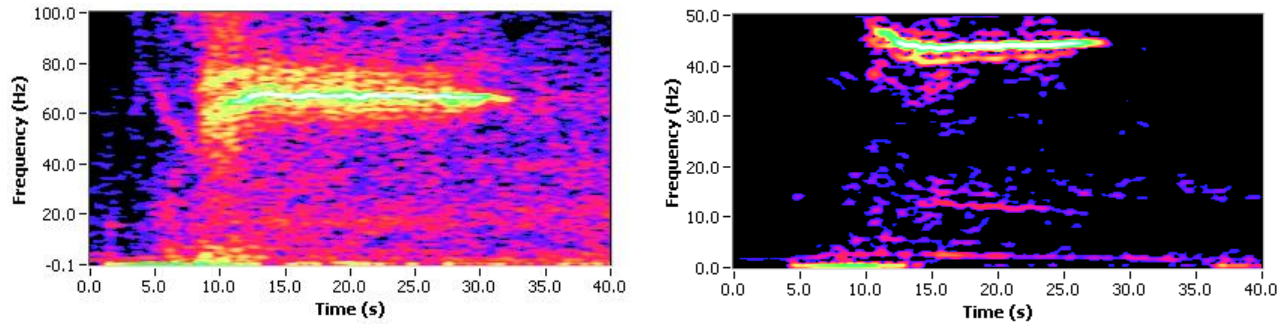

Figure 4: Case study 1 – Strain gauge blade 1, position 2, spectrogram (channel 44, NFFT = 512 samples) (left); Case study 2- Strain gauge signal blade 3, position A,
spectrogram (channel 52, NFFT = 256 samples) (right).

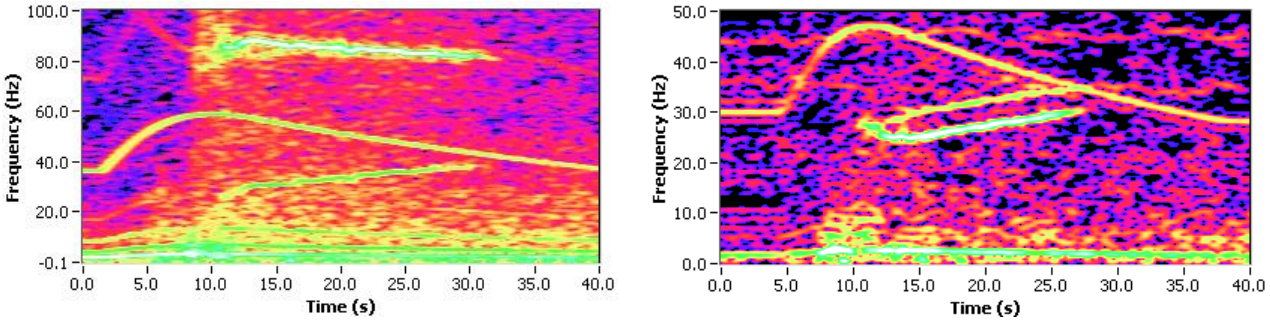

Figure 5: Case study 1 - Spectrogram of the labyrinth gap displacement 12 H (channel 37, NFFT = 512 samples) (left); Case study 2 - Spectrogram of the labyrinth gap displacement 12 H signal (channel 32, NFFT = 256 samples) (right**)**.

For case study 1, the vibration observed around 67 Hz in the rotating plane (Figure 4) appears in the static coordinates at 87.5 Hz for a rotating speed of 200 RPM (Figure 5, 16 s) and 82 Hz for a rotating speed of 154 RPM (Figure 5, 31 s). A second component is visible close to the second harmonic of the vibration phenomenon in the static coordinates but aliased in frequency (Figure 5, left). This second component starts around 28 Hz (14 s) to terminate at 38 Hz (31 s). Furthermore, a third component is visible on the whole length of time in Figure 5 (left) corresponding to the blade passing frequency. This component allows the estimation of the instantaneous RPM values deduced from the product of the blade passing frequency with the constant "60 s/17 blades". Note that the second harmonic visible on the labyrinth signal is not observed on the blade strain gauges. At the blade junction with the runner, facing the labyrinth, the tensile force transmits the vibration at its second harmonic through the labyrinth.

The blade vibration and a labyrinth gap displacement for case study 2 are shown respectively on the right of Figures 4 and 5. We observe the same frequency discrepancies as in case study 1 but combined with frequency aliasing of the main component. The vibration component observed at 43 Hz (14 s) to 44.3 Hz (26 s) in the rotating coordinate of the runner (Figure 4) has the non-aliased frequencies of 57 Hz and 55.7 Hz, respectively. Concurrently, the vibration phenomenon appears in the static coordinates (Figure 5) at the aliased frequencies of 24.5 Hz (14 s) for 161 RPM and 30 Hz (26 s) for 125.3 RPM, with the corresponding non-aliased frequencies of 75.5 Hz and 70 Hz. We observe a second component visible from 28 Hz (13 s) to 34 Hz (27 s) and a third component visible over the whole time length of the signal, which corresponds to the blade passing frequency.

In neither case study is the time-frequency resolution a concern. The observed modulation of the vibration components cannot be attributed only to the hydraulic inherent vortex random contribution. Some unsteady modulation is seen on the spectrogram of the gauge blade for case study 1 (Figure 4, left). This is even more obvious for case study 2, which exhibits a quasi-steady modulation over the whole duration of the phenomenon on the rotating and static coordinate reference measurement. The sidebands of the component measured by the blade strain gauge (Figure 4, right) have a steady 5-Hz distance (sideband to sideband) from 14 s to 26 s. This same 5-Hz distance is observed between the second and the main component in the static coordinates (Figure 5, right) although, without further modeling it is difficult to attribute physical meaning to this modulation and the corresponding frequency transfer from rotating to static coordinates.

5 Under-sampled signal correction (case study 2)

Even if the Nyquist rate is respected, as in case study 1, the cycle amplitudes obtained by rainflow counting can be underestimated if the acquisition frequency is not high enough. Interpolation can then be used to compensate for a low acquisition frequency in order to obtain more accurate values for the strain cycle maximums and minimums. However, if the signal is under-sampled, even with interpolation, the rainflow counting will obviously yield a wrong estimation of both the number of cycles and their amplitudes. In case study 2, our hypothesis is that the main component observed in the gauge strain signal is subjected to first-order aliasing, i.e. the original component is located between $[0.5f_s, 1.0f_s]$, where f_s is the sampling frequency. We propose to correct the under-sampled signal using the following methodology:

1. Parametric estimation of the component using the method developed for an AM-FM modulated sinusoid [6-9].
2. Subtraction of the estimated component from the signal.
3. Transformation of the estimated aliased component to estimate the unaliased component.
4. Addition of the unaliased component.

The transformation in step 3 is made by first considering a phase-time step $\theta_n - \theta_{n-1}$ from an aliased component described by:

$$a_n \cdot \cos(\theta_n) \tag{1}$$

where a_n is the estimated instantaneous amplitude, θ_n is the estimated phase and *n* is a time index. Next, because of the first-order aliasing hypothesis (2π radians missing for each time sample), we consider the unaliased phase step as:

$$\Delta\theta_n^u = \theta_n^u - \theta_{n-1}^u = (\theta_n - \theta_{n-1}) + 2\pi \tag{2}$$

which is interpolated $\Delta\theta_n^u \rightarrow \Delta\theta_i^u$ using the Shannon interpolation by the convolution of a windowed "sinc" function. The interpolated phase step values are then divided by the interpolation factor *k* to account for the shorter time step between samples as follows:

$$\Delta\theta_i = \frac{1}{k}\left(\Delta\theta_i^u\right),\ \Delta\theta_0 = 0.0 \tag{3}$$

and unwrapped to obtain:

$$\theta_I = \text{unwrap}(\Delta\theta_i) = \sum_{i=0}^{I} \Delta\theta_i \tag{4}$$

where θ_I is the interpolated unaliased instantaneous phase. Finally, the instantaneous amplitude is also *k*-interpolated $a_n \rightarrow a_I$ and the results from both are used to generate the estimated unaliased component described by:

$$a_I \cdot \cos(\theta_I) \tag{5}$$

The results obtained for case study 2 for an interpolation factor k=2 are shown in Figures 6 and 7. With an interpolation factor k=2, half of the corrected signal samples correspond to the aliased interpolated signal samples. The aliasing error can be observed in the other half of the corrected signal samples. The unaliased corrected signal can then be used to estimate the fatigue strain cycles. Note that the low-amplitude signal section before 12.5 s was not corrected since the parametric estimation failed to estimate this small-amplitude section of the component.

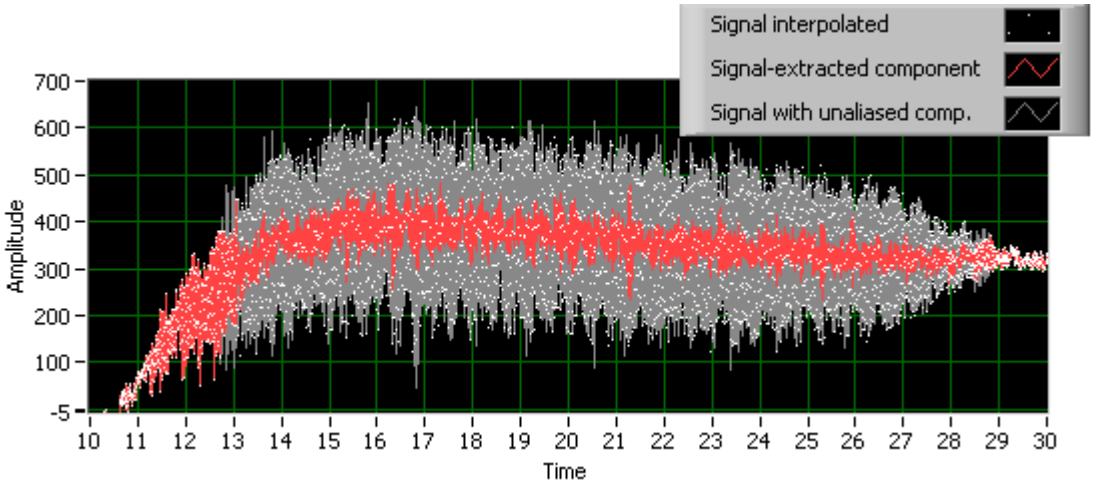

Figure 6: Aliased vs. unaliased signal for the strain gauge for case 1 - blade 1 - position 2. In red, the residual signal corresponding to the interpolated signal minus the estimated component.

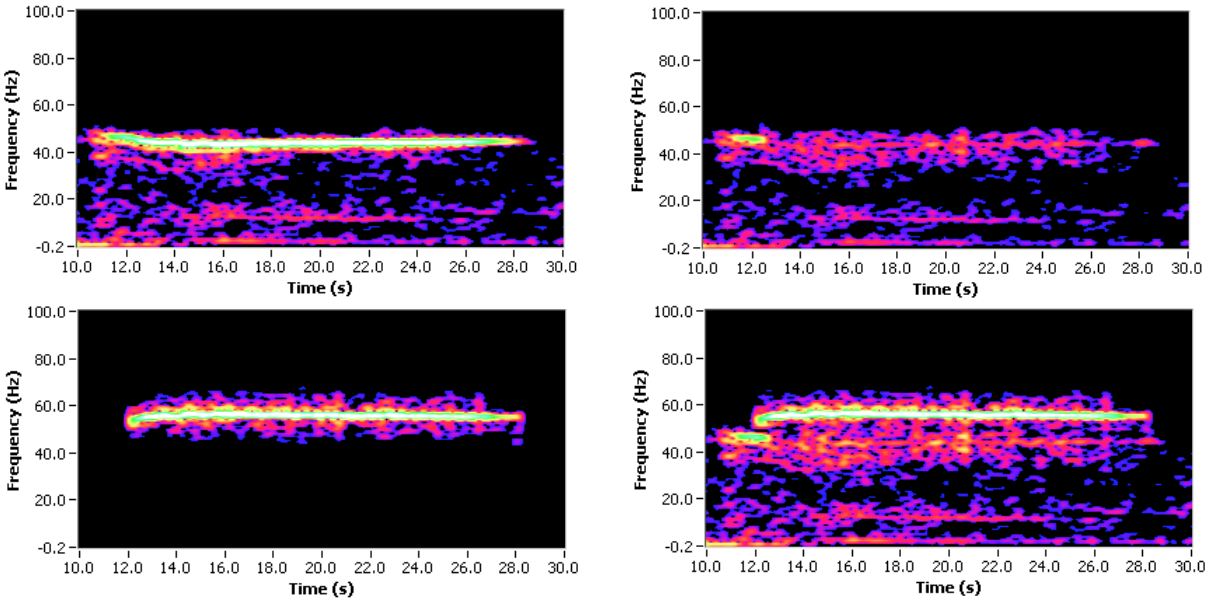

Figure 7: Four spectrograms: original interpolated (2x) signal, interpolated signal minus estimated component, unaliased estimated component and corrected signal.

6 Phase analysis

The cyclostationarity do not exhibit the same frequency between rotating and static components. Since frequencies are linked by the same cyclostationarity phenomenon, a phase relation exists between rotating and static components. However, in this paper, we will not discuss about this latter phase relation. Only the phase differences between sensors distributed in the same reference coordinates are considered (rotating or static).

Phase relations are estimated using dual-channel phase spectrograms [10-11]. A dual-channel phase spectrogram can reveal the phase difference between channels for all time-frequency pixels, whether constant frequencies are aligned or not. The dual-channel phase spectrogram for two different blades at the same blade location in case study 1 is shown in Figure 8. Note an approximately uniform phase relation around 130° through the entire component presented. In this case, considering all available combinations, we obtain an averaged phase difference of 128.6° between blades 1 and 2.

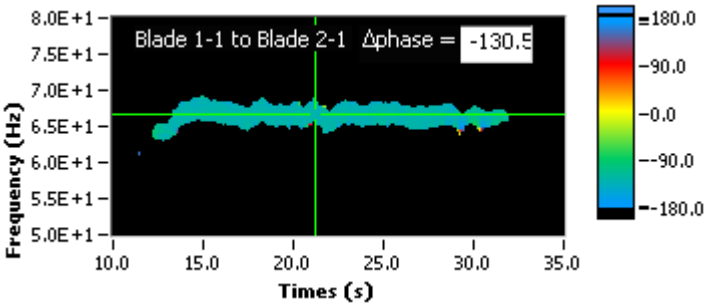

Figure 8: Case study 1 - Dual-channel phase spectrogram for blades 1 and 2, blade location 1 (ch.43-47, NFFT = 512 samples). The cursor read a -130.5° phase difference for the component shown.

The same can be obtained for labyrinth gap displacement. In Figure 9, the labyrinth gap displacement for transducers located at 90° from each other from case study 1 are presented. We observe a phase relation close to 180° on both the time signal and the dual-channel phase spectrogram.

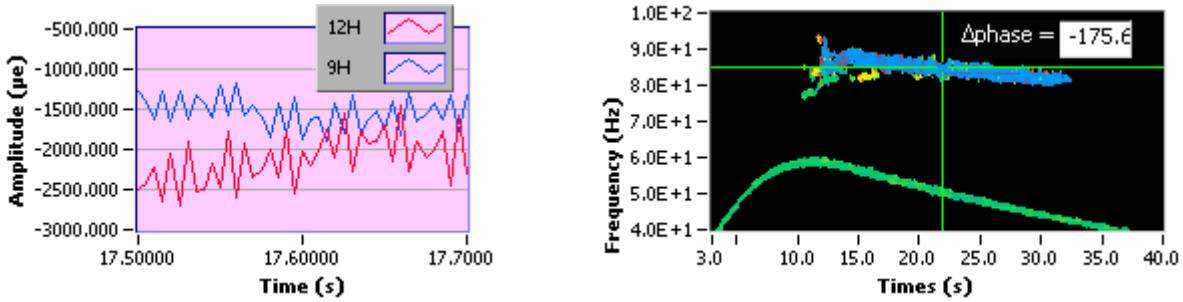

Figure 9: Case study 1 time signal of labyrinth gap displacement in 12 H and 9 H directions (left); corresponding dual-channel phase spectrogram of the main component (ch.37-38, NFFT = 512 samples) (right). The cursor dropped on the component read a -175.6° phase difference.

To increase the accuracy, we took the averages of every strain gauge location for four time steps. Table 1 shows the corresponding results with time averages and blade averages for case study 2. We observe that, for blades 3, 9 and 14, the average phase difference is -8.68°, -173° and 152°.

Ch.	Sensor location	Phase					
		16 s	18 s	20 s	24 s	Average	Blade average
52	Blade 3A reference	0°	0°	0°	0°	0°	-8.68°
53	Blade 3B	-6.2°	-4.92°	-4.81°	-4.76°	-5.13°	
54	Blade 3C	-5.18°	-4.29°	-3.91°	-3.74°	-4.28°	
55	Blade 3D	-27.05°	-24.93°	-25.04°	-24.24°	-25.31°	
56	Blade 9A	-154.71°	-155.86°	-161.01°	-163.31°	-158.72°	-173.06°
57	Blade 9B	-154.71°	-155.28°	-160.44°	-163.88°	-158.58°	
58	Blade 9C	-175.34°	-174.77°	-178.2°	-178.2°	-176.63°	
59	Blade 9D	161.59°	162.73°	160.8°	161.01°	161.69°	
60	Blade 14A	162.16°	165.02°	161.01°	157.58°	161.44°	152.24°
61	Blade 14B	157.00°	159.87°	157.00°	154.14°	157.00°	
62	Blade 14C	152.99°	156.43°	152.99°	150.70°	153.28°	
63	Aube 14D	136.37°	139.24°	137.52°	135.8°	137.23	

Table 1: Case study 2, 56-Hz component (44 Hz aliased frequency) phase differences from phase spectrogram

Note that for case study 2, in Figure 10, the dual-channel phase spectrogram of the labyrinth gap displacement for transducers at 90° to each other is close to 90°, which is different from case study 1. For our case studies, even if the strain responses look similar, we observe different structural behaviors.

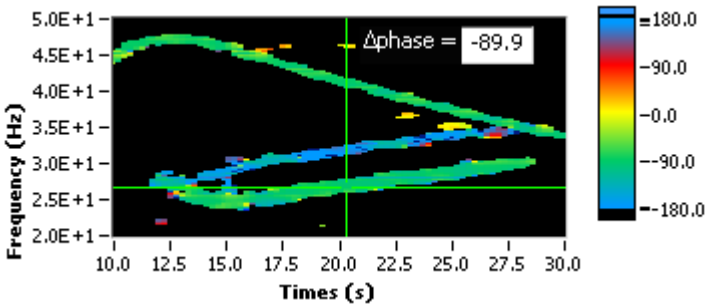

Figure 10: Case study 2, dual-channel phase spectrogram of the labyrinth gap displacement in 12 h and 3 h directions (channels 32-33, NFFT = 512 samples). The cursor dropped on the component read a -89.9° phase difference.

In order to understand the dynamic behavior of the two rotating structures, we use the following relation:

$$f_{stat} = N \text{ x } \left(\frac{f_{rot}}{N} \pm rpm / 60\text{s} \right) \tag{6}$$

which links the frequency f_{rot} of the rotating coordinates to the frequency f_{stat} of the static coordinate for a deformed shape having N nodes. The deformed shape can rotate in the reverse direction of the runner when - rpm/60 is applied, and in the same direction for + rpm/60. From this relation, we obtain two solutions for case study 1, both with six nodes, one rotating in the reverse direction and one rotating in the same direction of the runner. The reverse-direction solution implies the hypothesis of an aliased frequency component of 133 Hz instead of the 67-Hz component. The observed second harmonic of the 67-Hz component disqualifies this solution. We kept the solution rotating with the structure:

$$f_{stat} = 6 \text{ x } \left(\frac{67 \text{ Hz}}{6} + rpm / 60\text{s} \right) \tag{7}$$

which yields respectively 87 Hz for 200 RPM and 82.4 Hz for 154 RPM. These frequencies correspond to those observed at the labyrinth gap displacement (Figure 5 (left), 16 s and 31 s). Note that the rotating frequency of the 6-node pattern is 67 Hz/6 = 11.17 Hz. Furthermore, we observe in Figure 11 that a 180° phase difference between 9 h-12 h labyrinth is supported by the assumption of a 6-node pattern.

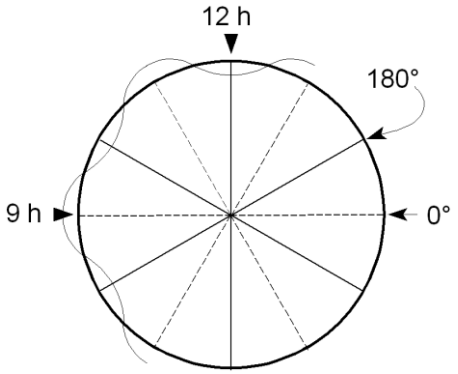

Figure 11: With a 6-node circular pattern, as in all 2N node patterns where N is odd, the phase is 180° shifted between two measurement points located 90° apart on the circumference.

In case study 2, the phase relations [-8.68°, -173°, 152°] can have two solutions, one with four nodes and another with seven nodes. Figure 12 illustrates the stroboscopic effect of 4-node and 7-node deformed shapes combined with the 17 blades of the runner. The red dots correspond to zero crossings on the blade periodicity (grey curve) and associated with the phase observed on the respective blade. The result obtained with a 7-node pattern ([-8°, -180°, 160°]) appears closer to the results observed on the blade phase measurements ([-8.68°,-173°,152°]). Moreover, Figure 13 shows that a 90° phase difference between the 12 h and 3 h labyrinth gap displacement channels is supported only by the 7-node pattern. For this case study, we retained the solution with the 7-node pattern rotating in the same direction as the runner. The solution of eq. 6 at 162.6 RPM (14 s) and the solution at 123.6 RPM (26 s) yield respectively 75 Hz and 70 Hz on the static coordinates. The frequencies are observed at the labyrinth gap displacement in Figure 5 (right) at 14 s and 26 s. Note that in case study 2 the rotation frequency of the 7-node modal pattern varies between 7.9 Hz and 8.2 Hz.

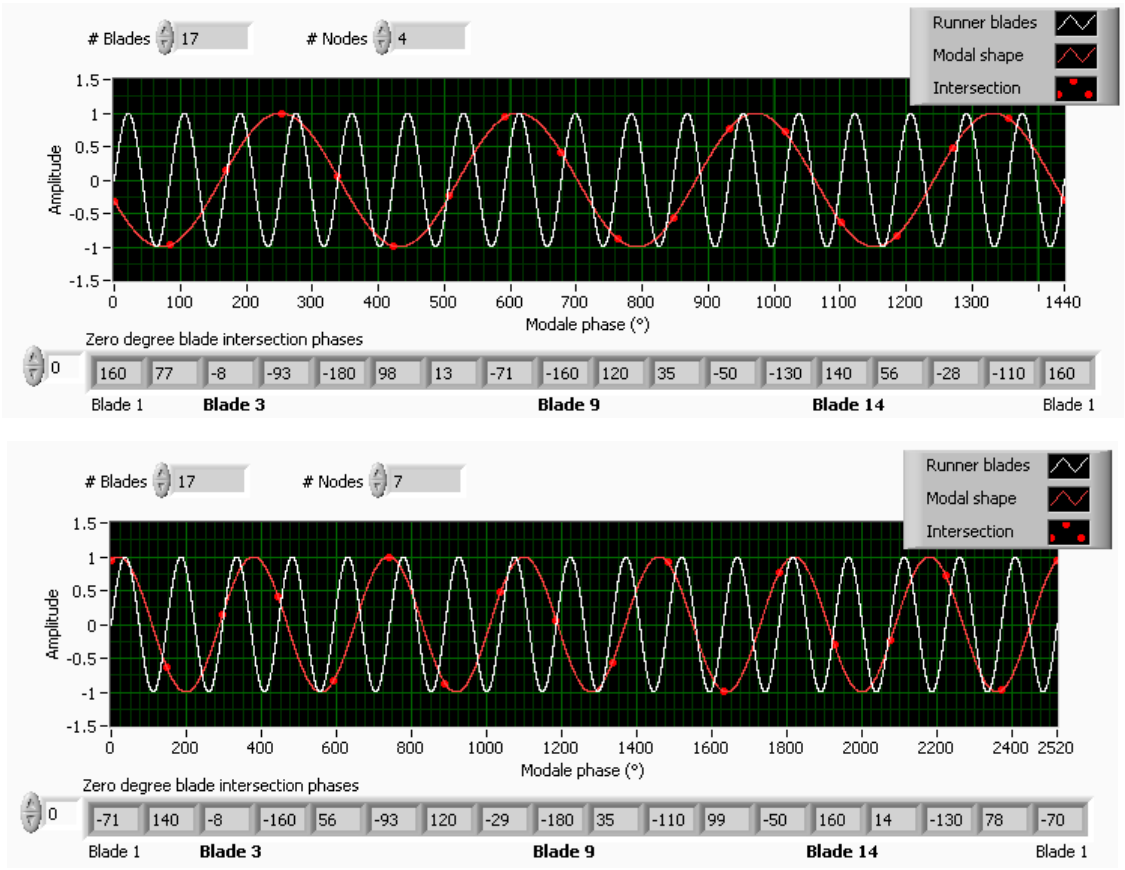

Figure 12: Blade phase observed for 4- and 7-node patterns. The blade 3 phase is fixed at -8° in accordance with the observed average reference phase listed in Table 1.

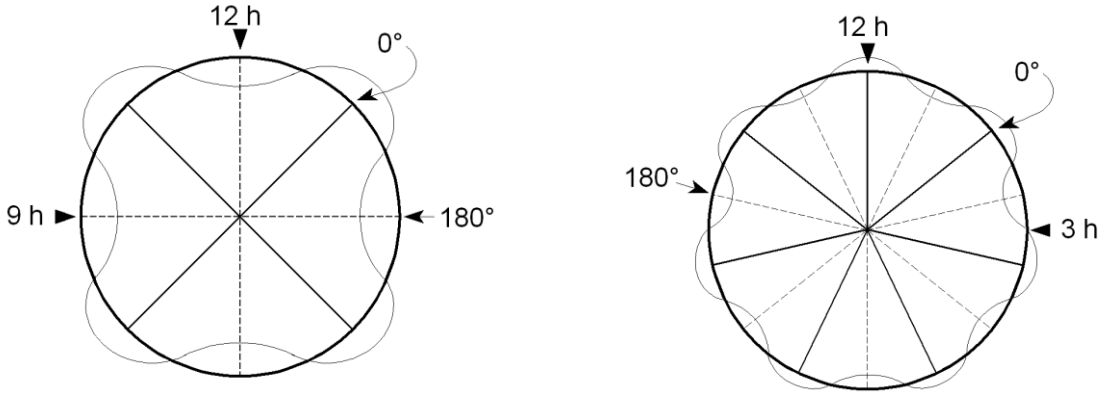

Figure 13: Four- (left) and 7- (right) node phase illustrations.

7 Influence on life assessment

The signal-processing methodology deployed to correct the aliased measurement in case study 2 combined with the interpolation of the unaliased vibration component enables a more accurate estimation of the actual rainflow cycle count, which can have a significant influence on life assessment using crack propagation. Figure 14 (right) presents a comparison between the load spectrum from the case study 2 aliased signal (see Figure 1) and the unaliased corrected results (see Figure 14, left).

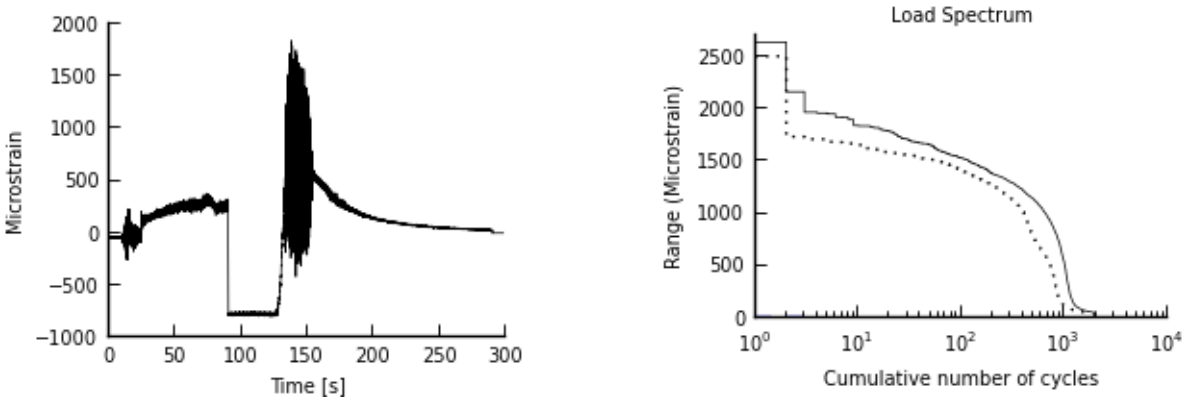

Figure 14: Case study 2. Unaliased interpolated signal (left); load spectrum comparison between the unaliased signal (continuous line) and original aliased signal (dotted line) (right).

We observe a significant increase in the amplitudes and number of cycles for the unaliased interpolated signal. This leads to an acceleration of the crack propagation speed, which can be observed in Figure 15. Notice that, even if the signal is not aliased, as in case study 1, the interpolation is still necessary to obtain an estimate of the correct amplitudes of the load spectrum because the main vibration component is close to the Nyquist rate.

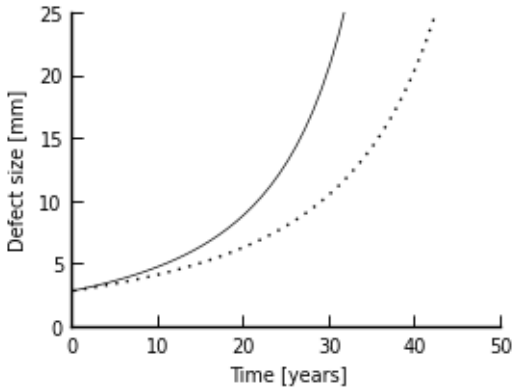

Figure 15: Comparison of the propagation results from the unaliased interpolated signal (continuous line) and the original aliased signal (dotted line).

8 Conclusions

In the two case studies presented, the vibration event generating most fatigue damage occurs during load rejection. In both cases, the high-level constraint seems to be generated by a sustained excitation of a fluid-structure resonance. The vibration analysis presented is able to link the frequencies observed in the rotating structure with those in the static coordinates. The vibration analysis shows a 6-node pattern for case study 1 and a 7-node pattern for case study 2. Both patterns rotate in the same direction of the wheel rotation. A special signal-processing methodology was used to correct the under-sampled measurement in case study 2. Using this methodology, the interpolated unaliased vibration component can be estimated accurately to obtain a suitable rainflow cycle count for fatigue analysis. Furthermore, to understand the dynamic behavior,

we identified the deformed shape observed with each case study to help develop numerical models for the whole rotating structure. From these models, a better understanding of the global behavior during the observed phenomenon and a more reliable estimate of life expectancy could be obtained.

References

[1] C. Trivedi, B. Gandhi, C. J. Michel, Effect of transients on Francis turbine runner life: a review, Journal of Hydraulic Research, 2013, 51, 121-132.

[2] M. Gagnon, S. A. Tahan, P. Bocher, D. Thibault, Impact of startup scheme on Francis runner life expectancy, IOP Conference Series: Earth and Environmental Science, 2010, 12, 012107.

[3] M. Gagnon, A. Tahan, P. Bocher, D. Thibault, On the stochastic simulation of hydroelectric turbine blades transient response, Mechanical Systems and Signal Processing, 2012, 32, 178 – 187.

[4] J. H. Gummer, S. Etter, Cracking of Francis runners during transient operation, International Journal on Hydropower & Dams, 2008, 4

[5] British Standards Institute, *Guidance on some methods for the assessment of flaws in welded construction*, BS7910, 2005

[6] F. Léonard, *La transformée en objets et les vers temps-fréquence*, Troisième conférence internationale sur les méthodes de surveillance et techniques de diagnostic acoustiques et vibratoires, held at CETIM in Senlis, France, October 1998.

[7] M. Jabloun, N. Martin, M. Vieira, and F. Léonard, *Maximum likelihood parameter estimation of short-time multicomponent signals with nonlinear AM/FM modulation*, in Proc. IEEE Workshop Statist. Signal Processing, Bordeaux, France, July, 2005.

[8] M. Jabloun, F. Léonard, M. Vieira, and N. Martin, *New flexible approach to estimate the IA and IF of nonstationary signals*, IEEE Transactions on Signal Processing, Vol. 55, No. 7, July 2007.

[9] M. Jabloun, N. Martin, F. Leonard, M. Vieira, *Estimation of the instantaneous amplitude and frequency of non-stationary short-time signals*, Signal Processing, 2008, 88, 1636 – 1655.

[10] F. Léonard, *Spectrogramme de phase et spectrogramme de fréquence*, Revue Traitement du Signal, Vol. 17, No.4, p 269-286, 2000.

[11] F. Léonard, *Phase spectrogram and frequency spectrogram as new diagnostic too*ls, Mechanical Systems and Signal Processing, 2007, 21, 125-137.